Effect of Ni content on 475°C embrittlement of directed energy deposited duplex stainless steel using a laser beam and wire feedstock

N.B. When citing this work, cite the original published paper.

(article starts on next page)

Full Length Article

Effect of Ni content on 475°C embrittlement of directed energy deposited duplex stainless steel using a laser beam and wire feedstock

Amir Baghdadchi [a,*], Mattias Thuvander [b], Sten Wessman [a], Boian T. Alexandrov [c], Joel Andersson [a]

[a] Department of Engineering Science, University West, 461 86, Trollhättan, Sweden
[b] Department of Physics, Chalmers University of Technology, SE-412 96, Göteborg, Sweden
[c] Department of Materials Science and Engineering, The Ohio State University, Columbus, OH 43221, USA

ARTICLE INFO

ABSTRACT

Duplex stainless steel (DSS), specifically the 2209 grade, is increasingly employed in additive manufacturing, particularly in processes like directed energy deposition using a laser beam with wire (DED-LB/w). However, a significant challenge arises when DSS faces brittleness within the temperature range of 250–500 °C. This study employs advanced characterization techniques, including atom probe tomography (APT) and transmission electron microscopy (TEM), to investigate DSS embrittlement after aging at 400 °C for up to 1000 h. The hardness analysis revealed that the higher Ni content in DED-LB/w-fabricated DSS cylinder promotes the age hardening compared to 2205 wrought DSS plate. Furthermore, APT and TEM demonstrated that, alongside the decomposition of ferrite into Fe-rich (α) and Cr-rich (α') phases, clustering of Ni, Mn, and Si atoms contributes to the embrittlement. Although the Ni-Mn-Si-rich clusters could suggest nucleation of G-phase, the G-phase crystal structure was not observed by TEM. This might be attributed to the short aging time or limitations in the characterization technique. This work underscores the impact of characterization techniques on the measurement of spinodal decomposition, with APT providing capability of detecting nanometer sized clusters. By elucidating the complexities of 475 °C-embrittlement in DED-LB/w DSS, this study offers valuable insights for industrial applications and a deeper understanding of age hardening in duplex DSSs under specific manufacturing conditions.

1. Introduction

Duplex stainless steels (DSSs) exhibit a two-phase microstructure, consisting of approximately equal fractions of austenite and ferrite. Thanks to their high corrosion resistance and good mechanical properties, DSSs find widespread applications across industries like, oil and gas, petroleum refining, chemical manufacturing, and nuclear energy. However, a significant challenge arises when DSSs are exposed to temperatures within the range of 250–500 °C. This occurs due to the decomposition of the ferrite phase into Fe-rich (α) and Cr-rich (α') phases, a phenomenon known as 475 °C-embrittlement, as it exhibits the most rapid embrittlement kinetics at 475 °C. The decomposition of ferrite occurs as a result of the presence of a miscibility gap within the Fe-Cr system and can occur through either nucleation and growth or the spinodal decomposition mechanism. In the presence of other alloying elements like Ni, Mn, Mo, and Si, age hardening of DSS at 475 °C can

also be the result of the formation of additional intermetallic compounds, such as G-, R-, or χ-phase [1–3].

The advent of additive manufacturing (AM) has opened up new avenues for producing nearly fully shaped components of DSS, offering reduced material waste, tailored properties, and intricate designs. Directed energy deposition using a laser beam with wire feedstock (DED-LB/w), also known as laser metal deposition with wire (LMDw), is an AM technique that utilizes a laser beam energy source to melt the wire feedstock, enabling the deposition of material layer by layer to construct the desired component. The rapid cooling rate inherent to the DED-LB/w process, however, hinders sufficient austenite formation, resulting in a prevalence of high ferrite fractions within additively manufactured DSS components. Unfortunately, this dominance of ferrite can detrimentally affect the toughness and corrosion resistance of these materials. To counteract the effects of the rapid cooling, specially formulated filler materials (with 2–4% higher Ni content), originally designed for

* Corresponding author.
  E-mail address: amir.baghdadchi@hv.se (A. Baghdadchi).

welding, have been utilized for AM applications. In addition to creating an unbalanced microstructure, the high cooling rate of DED-LB/w causes limited partitioning of alloying elements in ferrite and austenite [4]. Consequently, the ferrite present in additively manufactured DSS exhibits notably higher Ni content compared to the ferrite in wrought DSS.

There have been many studies on the 475 °C embrittlement in DSS, and some have explored DSS welds. However, a research gap exists regarding the investigation of 475 °C embrittlement in additively manufactured DSS. Several investigations [3,5,6] have highlighted the influential role of Ni in promoting age hardening of DSS when exposed to temperatures ranging from 200 °C to 500 °C. Zhou et al. [5] investigated the effect of chemical composition on the kinetics of phase separation in DSS welds. Their findings revealed a more pronounced phase separation and clustering of Ni-Mn-Si-Cu in the weld metal, attributed to the higher Ni content. Garfinkel et al. [6] conducted a study on age hardening of both wrought and welded DSS at 427 °C, revealing the role of Ni and Mo in the formation of G-phase, which leads to age hardening of the ferrite phase. Sakata et al. [3] provided evidence that an increased Ni content accelerates spinodal decomposition and the formation of solute clusters, thus contributing to age hardening of the ferrite in multi-pass welding of DSS. All three of these studies were in agreement that a higher Ni content promotes the decomposition of ferrite into α and α' phases. Additionally, in conjunction with the presence of Mn and Si, it triggers the formation of G-phase [7].

Among DSS grades, 2205 DSS, containing roughly 22% Cr, stands out as a favored choice thanks to the beneficial combination of corrosion resistance, strength, toughness, and cost-effectiveness. The designated filler material for welding this grade is 2209 DSS, which belongs to the same 22% Cr category. However, it has 4% higher Ni content, aimed at promoting the formation of austenite during the welding process. The utilization of 2209 DSS has extended to the realm of AM, particularly when utilizing wire as feedstock material. However, a gap exists in the understanding of the age-hardening behavior of additively manufactured DSS components, specifically regarding the 475 °C embrittlement phenomenon. The objective of this study, therefore, is to compare the age-hardening behavior of a DED-LB/w component fabricated using 2209 DSS wire, which has high Ni content, and 2205 wrought DSS plate. Atom probe tomography (APT) and transmission electron microscopy (TEM) were employed to elucidate the age-hardening mechanisms of DSS fabricated by the DED-LB/w process with enhanced Ni content. In summary, this study aims to provide insights into the age-hardening behavior of additively manufactured DSS components, contributing to the optimization of AM processes and the development of high-performance materials for various industrial applications.

2. Experimental

2.1. Materials

In this study, an additively manufactured cylinder with 2209 DSS (EN ISO 14,343-A: G 22 9 3 N L) wire and conventionally wrought 2205 DSS (UNS S32205) plate were utilized. The 2209 DSS cylinder, as illustrated in Fig. 1-a, was fabricated through DED-LB/w, revealing a layer-by-layer microstructure, as shown in Fig. 1-b. Within this microstructure, the darker regions primarily comprises ferrite, while the brighter regions contain a significant fraction of austenite [8]. Based on the phase map extracted from electron backscatter diffraction (EBSD) analysis of the top layer deposited bead, the microstructure is predominantly ferritic, as depicted in Fig. 1-c. More details about the fabrication of the cylinder can be found in Ref. [8]. The microstructure of the 2205 wrought DSS is also depicted in Fig. 1-d. As evident, the microstructure consists of elongated ferrite and austenite grains, at about 50% each. The
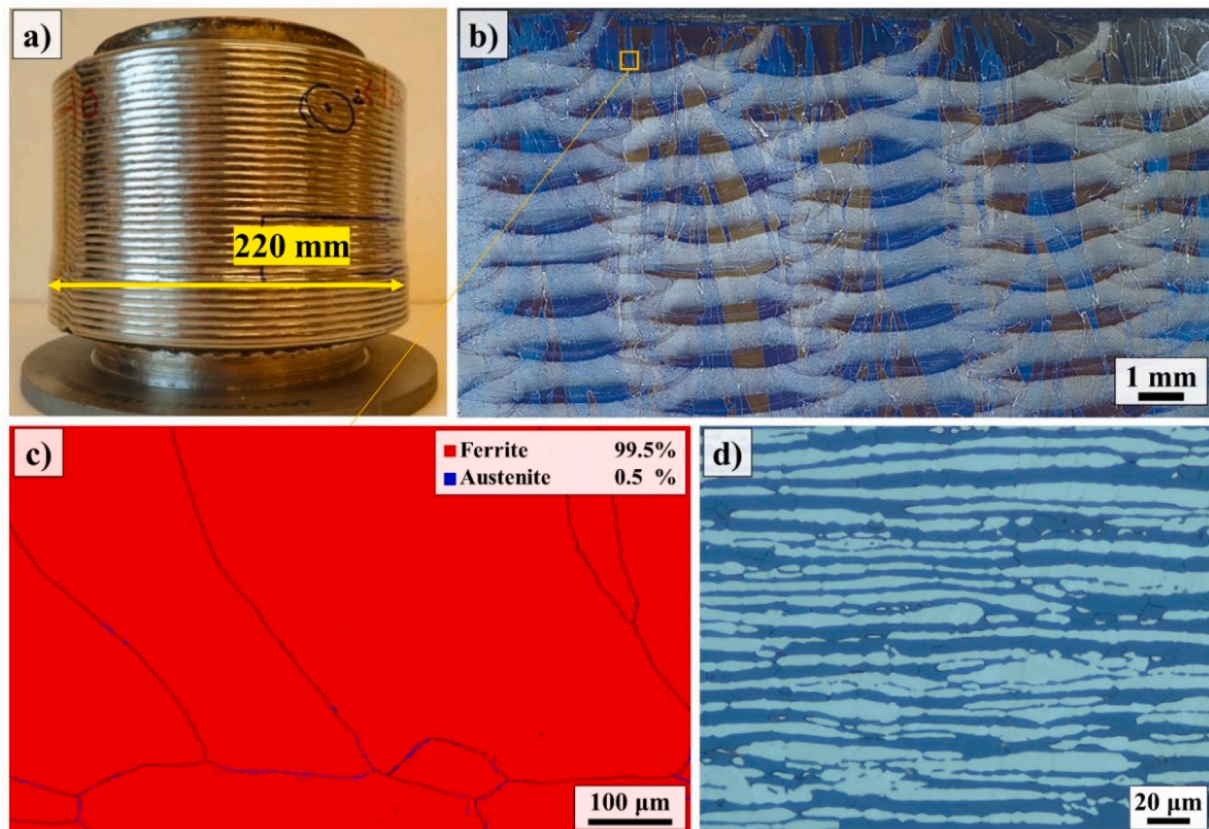
Fig. 1. a) Additively manufactured cylinder by DED-LB/w, b) layer by layer microstructure of the cylinder (The darker areas consist mainly of ferrite, whereas the brighter regions contain a high fraction of austenite), c) phase map of last layer (almost fully ferritic microstructure with less than 1% austenite at ferrite/ferrite grain boundaries), and d) 2205 wrought DSS plate microstructure consisting of elongated ferrite and austenite grains.

chemical composition of the wrought 2205 DSS and the additively manufactured cylinder, as provided by the material producer certificate and a prior study [8], respectively, is outlined in Table 1. It should be mentioned that nitrogen loss during the DED-LB/w process resulted in a lower nitrogen content in the cylinder compared to feedstock 2209 wire [9].

2.2. Aging heat treatment

The 2209 DED-LB/w DSS cylinder and the 2205 wrought DSS plate underwent isothermal aging at 400 °C for durations of 10, 50, 200, and 1000 h in an ambient atmosphere, followed by air cooling. The selection of the aging temperature was motivated by the existing body of research conducted using this temperature, which in turn facilitates a meaningful comparison of the performance of DED-LB/w components and those produced using conventional fabrication methods [10,11]. The choice of aging durations was based on previous studies that have commonly investigated aging behaviors within these timeframes to assess the evolution of the microstructure and the mechanical properties [10].

2.3. Vickers microhardness test

The Vickers hardness measurements were carried out to assess the age hardening of ferrite after different aging durations. For this purpose, a Struers Duramin-40 instrument was utilized, applying a load of 10 gf (gram-force) for a dwell time of 10 s. The reported hardness value for each sample represents an average of at least 10 measurements specifically on the ferrite phase.

2.4. Microstructure characterization

The DED-LB/w aged samples were analyzed by APT and TEM. The APT provides precise chemical composition analysis at the atomic level, making it ideal for analyzing nano-scale phenomena such as the decomposition of ferrite and clustering of Ni, Mn, and Si atoms. However, APT does not provide information about the crystal structure. To address this limitation, TEM analysis was performed to gain insights into the crystal structure of the material.

For APT, rods with dimensions of $0.3 \times 0.3 \times 15$ mm^3 were extracted via high precision cutting from ferritic areas of the DED-LB/w component. The middle of the rods was subjected to an electropolishing procedure, resulting in the creation of two needle-shaped specimens. The electropolishing procedure encompassed two stages at a voltage of 22 V. The initial stage employed an electrolyte consisting of 10% perchloric acid, 20% glycerol, and 70% ethanol, followed by a second stage utilizing an electrolyte consisting of 2% perchloric acid and 98% 2-butoxyethanol. APT was done with a pulse fraction of 20%, at a temperature of 70 K. A local electrode atom probe, LEAP 6000 XR (Cameca), was employed. The software AP Suite 6.3 was used to reconstruct and analyze the APT data.

The approach introduced by Zhou et al. [5,12] using the radial distribution function (RDF) was used to determine the wavelength and the amplitude of the spinodal decomposition. The RDF can be used to detect phase separation. The RDF represents the average radial concentration profile starting from each and every detected atom of the selected element. The measured concentration at each position was normalized with respect to the average bulk concentration. The RDF can be expressed as:

$$RDF(r) \; = \; C_E(r)/C_0 \; = \; (N_E(r) \, / \, N(r))/C_0$$

where $C_E(r)$ is the composition of element E at a distance r, C_0 is the average composition of element E in the analyzed volume, $N_E(r)$ is the total number of atoms of element E at a distance r, and $N(r)$ is the total number of atoms of all elements at a distance r. The spinodal amplitude, which is the Cr amplitude, can be estimated by RDF_{Cr} at zero distance, which is determined by extrapolating the RDF curve to zero distance. The amplitude of the spinodal decomposition is:

$$Amplitude = C_0\sqrt{2(RDF_{Cr}(0) - 1)}$$

The wavelength was estimated by the distance of the first local maximum in the bulk normalized RDF_{Cr} curve. For providing three-dimensional (3D) isoconcentration surfaces, the thresholds of 63 at.% Fe, 31 at.% Cr, and 20 at.% Ni+Mn+Si were used for Fe-rich, Cr-rich, and Ni-Mn-Si- rich volumes, respectively.

For TEM analysis, the sample extraction was carried out using the focus ion beam (FIB) technique [13]. The Helios NanoLab 600 equipped with a field emission gun (FEG) electron source was used for FIB extraction. Initially, a thin foil with an approximate thickness of 1 μm was extracted from a region exhibiting complete ferritic microstructure. After that, the foil underwent FIB thinning, reducing its thickness to below 100 nm. The Titan 60–300 TEM with a high coherence field emission electron gun (X-FEG) and the Tecnai F20 were used to get energy dispersive spectroscopy (EDS) and diffraction patterns to analyze the chemical composition and crystal structure, respectively.

3. Results

In this section, firstly hardness analyses of both the 2205 wrought DSS plate and the 2209 DED-LB/w DSS cylinder are presented. Following this, a comprehensive exploration of the 2209 DED-LB/w DSS is provided through APT and TEM analyses with more details.

3.1. Hardness analysis

The Vickers microhardness results for the ferrite phase in the 2205-wrought DSS plate and 2209 DED-LB/w DSS cylinder are presented in Fig. 2. Precise hardness measurements were performed by positioning indentations completely in the ferrite phase as depicted in Fig. 3 to prevent any influence from the austenite. Furthermore, the smallest indentations were used, thus minimizing the potential influence of austenite that might be present in the underlying layers.

Before aging, the hardness of 2205-wrought DSS was 317 HV while the hardness of 2209- DED-LB/w DSS was 349 HV. Upon aging at 400 °C, consistently across all aging dwell times, the hardness of the DED-LB/w sample surpasses that of the wrought counterpart. Comparing the aging of the two samples after 10 hour dwell time, the DED-LB/w sample exhibits accelerated age hardening kinetics during the initial stages of aging. Following 1000 h of aging, the ferrite hardness in the 2205-wrought DSS measures at 480 HV, while the 2209- DED-LB/w DSS exhibits a value of 564 HV.

3.2. Atom probe tomography

The APT technique is highly sensitive for detecting the early stages of spinodal decomposition as well as clustering. As the increase in hardness observed above can be expected to be a result of these phenomena, the

Table 1
Chemical composition of the 2205 wrought and 2209 DED-LB/w DSS (wt.%).

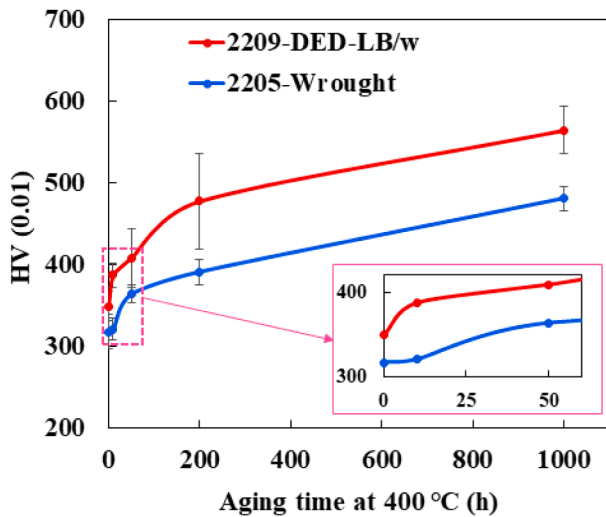|	C	Si	Mn	P	S	Cr	Ni	Mo	Cu	N
2205 wrought DSS plate	0.016	0.32	1.77	0.027	<0.001	22.77	5.50	3.07	0.21	0.18
2209 DED-LB/w DSS cylinder	0.014	0.48	1.42	0.018	<0.002	23.54	8.30	3.32	0.06	0.11

Fig. 2. Vickers hardness of the ferrite phase in 2209 DED-LB/w DSS cylinder and 2205 wrought DSS plate after aging at 400 °C.

aged AM material was investigated using APT after different aging times.

The isoconcentration surfaces depicting the Fe-rich, Cr-rich, and Ni-Mn-Si-rich regions within the ferrite of DED-LB/w samples after aging at 400 °C for 10, 50, and 1000 h, as observed in the APT analysis, are presented in Fig. 4. Atom maps of Ni, Mn, and Si in 5 nm thick slices of the APT reconstructions are shown in Fig. 5. These findings illustrate that the decomposition of ferrite into Fe-rich (α) and Cr-rich (α') phases initiates after just 10 h of aging at 400 °C. However, as Fig. 4-b demonstrates, there is no noticeable clustering of Ni, Mn, and Si atoms after 10 h of aging.

With aging continuing to 50 h, both the Fe-rich and Cr-rich phases grow larger. Moreover, there are several Ni-Mn-Si-rich clusters of varying sizes that become apparent at the interfaces of the Fe-rich and Cr-rich phases. It is also notable in Fig. 5, that the Ni, Mn, and Si atoms accumulate in the same regions. It is important to note that Fig. 4 represents 3D maps, while a very thin slice (5 nm) was selected to display the atom maps in Fig. 5. Therefore, Fig. 5 can be considered as 2D representations.

Following 1000 h of aging, not only does the number of Ni-Mn-Si-rich particles significantly increase, but they also tend to exhibit a more uniform size. A 5 nm-thick cross-sectional view of these atom
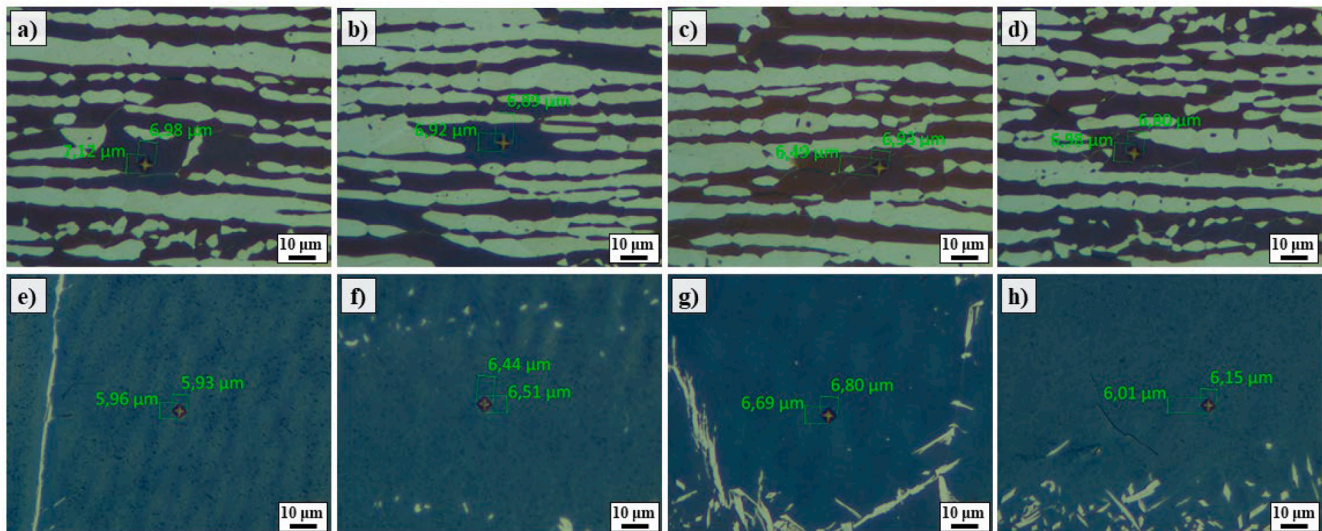

Fig. 3. Vickers microhardness indentations of the ferrite phase in (a-d) 2205 wrought DSS plate, and (e-h) 2209 DED-LB/w DSS cylinder after 200-hour aging at 400 °C. Care was taken to position the indentations within the ferrite phase, thus avoiding any influence from the austenite phase.
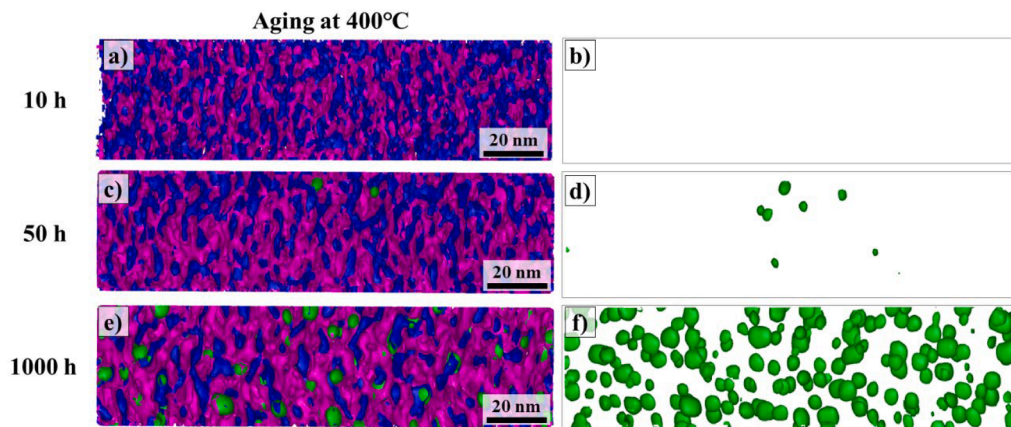

Fig. 4. Iso-concentration surfaces illustrating Fe-rich regions (> 63 at. %) in purple, Cr-rich regions (> 31 at. %) in blue, and Ni-Mn-Si-rich regions (> 20 at. %) in green and the depiction of only Ni-Mn-Si 20% iso-concentration surfaces after (a, b) 10 h, (c, d) 50 h, and (e, f) 1000 h of aging. It can be seen that the spinodal wavelength and the clustering increase with time.
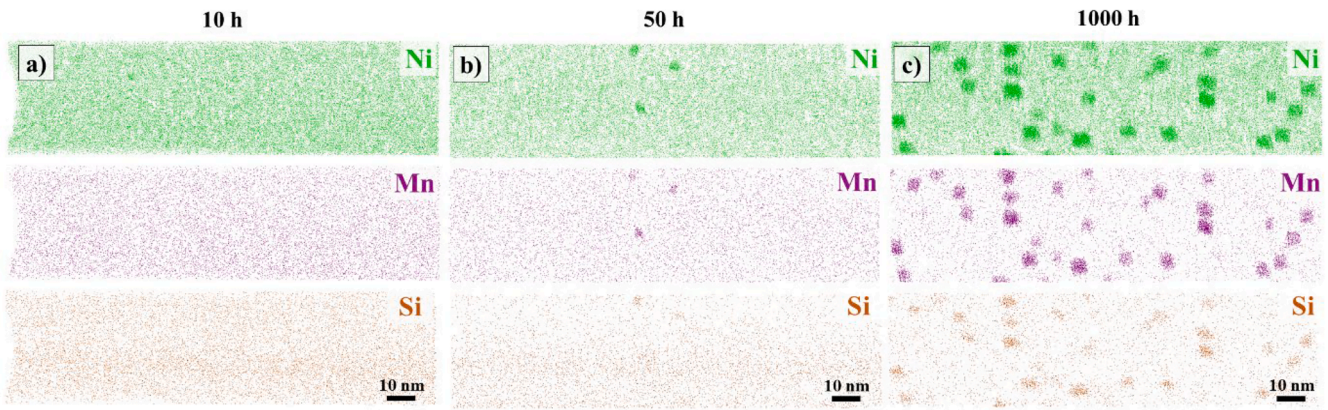
Fig. 5. The distribution of all Ni, Mn, and Si atoms within a 5 nm-thick slice following (a) 10 h, (b) 50 h, and (c) 1000 h of aging.

maps, depicted in Fig. 5-c reveals the concentration of Ni, Mn, and Si atoms in identical positions. This cross-section also provides insights into how the extended aging time leads to the formation and growth of these clusters (or very small precipitates).

The normalized Cr-Cr RDF curves, as shown in Fig. 6, provide a clear representation of how the phase decomposition becomes more pronounced with increasing aging time. As explained earlier, the wavelength and amplitude of the spinodal decomposition were determined from these Cr-Cr RDF curves and are presented in Table 2.

Fig. 7 presents the concentration profile of the Cr-rich regions after aging for 1000 h. The graphs are called proximity histograms (proxigrams), which are concentration profiles relative to isoconcentration surfaces (isosurfaces). It is important to note that, in this representation, positive distances correspond to inside the Cr-rich regions, while negative distances correspond to the outside of these regions. Within the Cr-rich regions, a notable enrichment of Cr atoms is observed, while there is a concurrent migration of Fe atoms away from the Cr-rich (α') phase. Furthermore, it becomes evident that other alloying elements such as Ni, Mn, and Si start to leave the α' phase. Consequently, there is an enrichment of Ni, Mn, and Si atoms outside the α' phase.
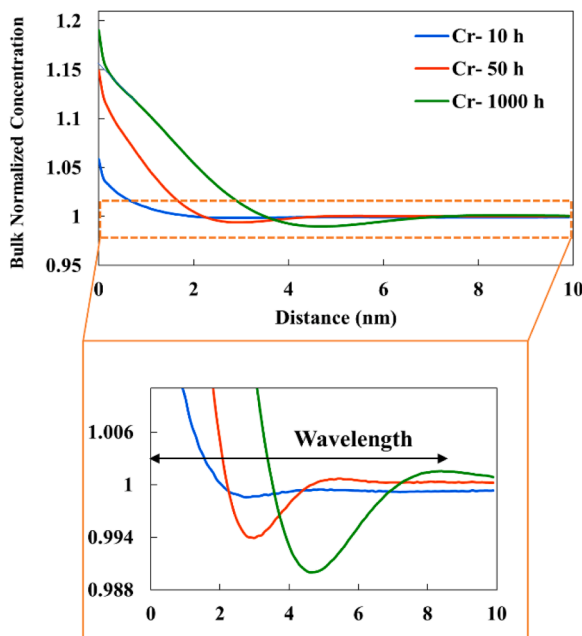
Table 2
The wavelength and amplitude of ferrite decomposition into Fe-rich and Cr-rich phases after 10, 50, and 1000 h aging at 400 °C.

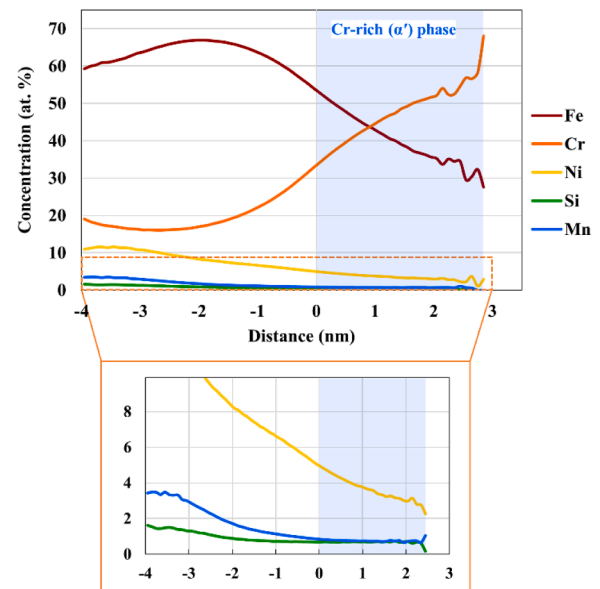|	Aging condition	Wavelength (nm)	Amplitude (at.%)
DED-LB/w −2209	10 h	4.9	9
	50 h	5.5	13.7
	1000 h	8.4	14.6

Fig. 7. Chemical composition of the Cr-rich regions after aging for 1000 h This figure illustrates the diffusion of Fe from the Cr-rich region, and notably, the migration of other alloying elements such as Ni, Mn, and Si out of the Cr-rich region.

In Fig. 4, the results at the 50-hour aging reveal spinodal decomposition of ferrite into Fe-rich and Cr-rich phases, accompanied by the emergence of clusters enriched with Ni, Mn, and Si. This observation is supported by the absence of a strong Cr depletion around the Cr-rich region (Fig. 7), indicating that spinodal decomposition is the predominant mechanism. Fig. 8 provides a depiction of the chemical composition across the interface and the cluster sizes after both 50 h and 1000 h of aging. After 50 h aging at 400 °C, the Ni content within the clusters exhibits a gradient, with higher concentrations toward the center, surpassing that of Fe and Cr. A similar trend is observed for Mn and Si, although their concentrations are lower compared to Ni. Moreover, Ni,
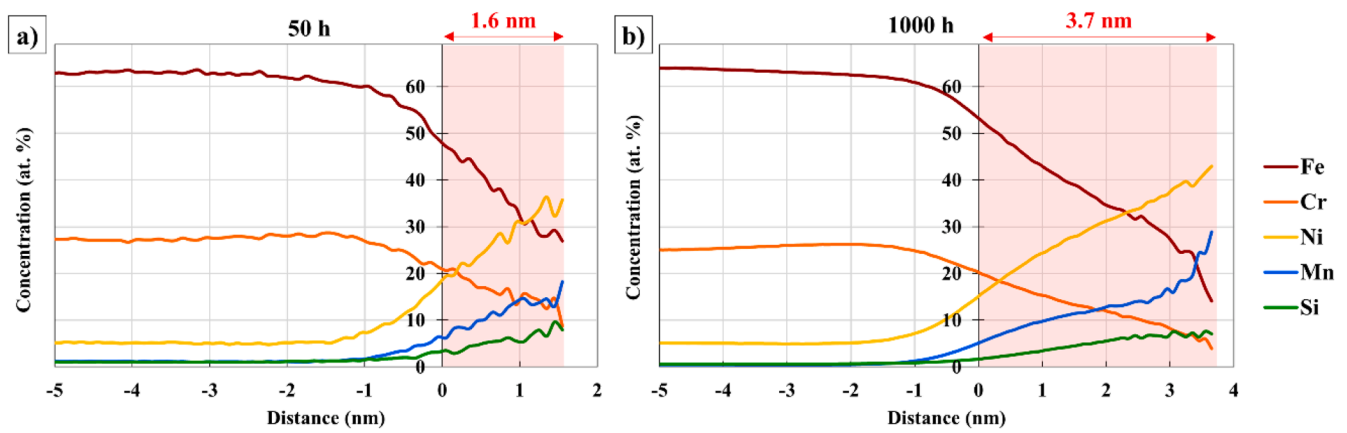

Fig. 6. The Cr-Cr RDF of 2209-DED-LB/w samples after 10, 50, and 1000 h aging at 400 °C. The arrow marks the wavelength of the sample aged for 1000 h.

Fig. 8. Proxigrams of Ni-Mn-Si-rich clusters after a) 50 h, and b) 1000 h aging at 400 °C.

Mn, and Si atoms accumulate within the cluster, while Fe and Cr atoms depart from it. It is worth noting that the clusters still consist of approximately 50% matrix elements i.e., Fe and Cr. After 1000 h of aging, the clusters grow, reaching a radius of about 3.7 nm. At the center of these clusters, the Ni content increases to around 40%. Furthermore, there are substantial increases in Mn and Si atomic percentages, particularly in the case of Mn. Matrix elements like Fe and Cr also are still observed within the clusters.

As previously mentioned, the Ni, Mn, and Si content did not reach the 20% threshold necessary for display in Fig. 4-b after 10 h of aging. However, the normalized Ni-RDF curves presented in Fig. 9 clearly demonstrate that the accumulation of Ni atoms starts at the early stages of aging, as evident after just 10 h.

The size distribution of the Ni-Mn-Si-rich clusters after 1000 h of aging at 400 °C, using isosurfaces, is presented in Fig. 10. It is assumed that the smallest volume of the cluster is 1 nm^3, which corresponds to a minimum radius of about 0.6 nm. It is evident that the majority of clusters have radii in the range of approximately 2–3 nm.
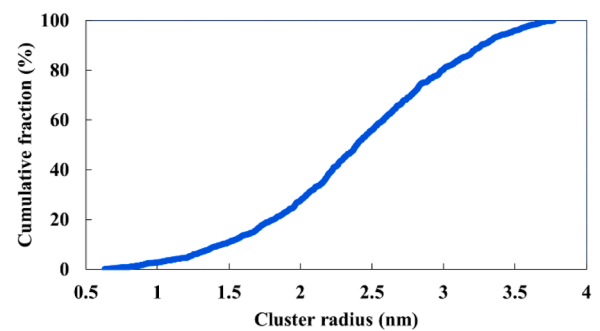

Fig. 10. Cumulative size distribution of Ni-Mn-Si-rich clusters after aging for 1000 h.

3.3. Transmission electron microscopy

Transmission electron microscopy (TEM) analysis was conducted to confirm the ferrite decomposition and the clustering of Ni-Mn-Si atoms observed by APT, and to attempt to determine the crystal structure of the clusters.

The elemental distribution maps of Fe, Cr, Ni, Mn, Mo, and Si in the ferrite of the DED-LB/w sample after 1000 h aging at 400 °C are shown in Fig. 11. It can be seen that the distribution of alloying elements in the ferrite is not homogeneous. A more detailed inspection reveals distinct Cr-rich regions (one such region is marked by the orange arrow), coinciding with a diminished Fe content. Moreover, such regions do not exhibit a significant accumulation of other alloying elements, including Ni, Mn, and Si. Moreover, areas characterized by the accumulation of Ni, Mn, and Si atoms (the yellow arrow highlights one such area), concomitant with a depletion of Fe and Cr atoms. Hence, the orange arrow denotes the decomposition of ferrite into Fe-rich and Cr-rich regions, while the yellow arrow indicates the accumulation of Ni, Mn, and Si at the interface of Fe-rich and Cr-rich areas.

An attempt was made to obtain crystallographic information of the presumed G-phase formation using selected area electron diffraction (SAED) analysis of the DED-LB/w sample after 1000 h of aging at 400 °C. Fig. 12-a shows an overview TEM image of the thin foil extracted from the ferritic region using FIB. The foil contains a hole. Diffraction patterns were obtained from two areas around the hole, as these regions are very thin making it more suitable for detecting very small phases. The indexed SAED patterns, shown in Figs 12-b and 12-c, are from the [011] and [001] zone axis, respectively. It should be noted that the crystal structure of the matrix is body-centered cubic (bcc), while the G-phase crystal structure is cF116, a face-centered cubic (fcc) lattice with a lattice parameter exactly four times that of the bcc ferritic matrix. G-phase
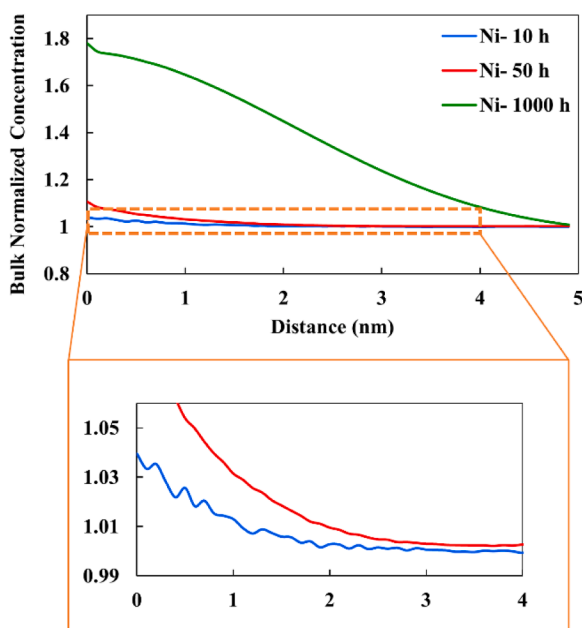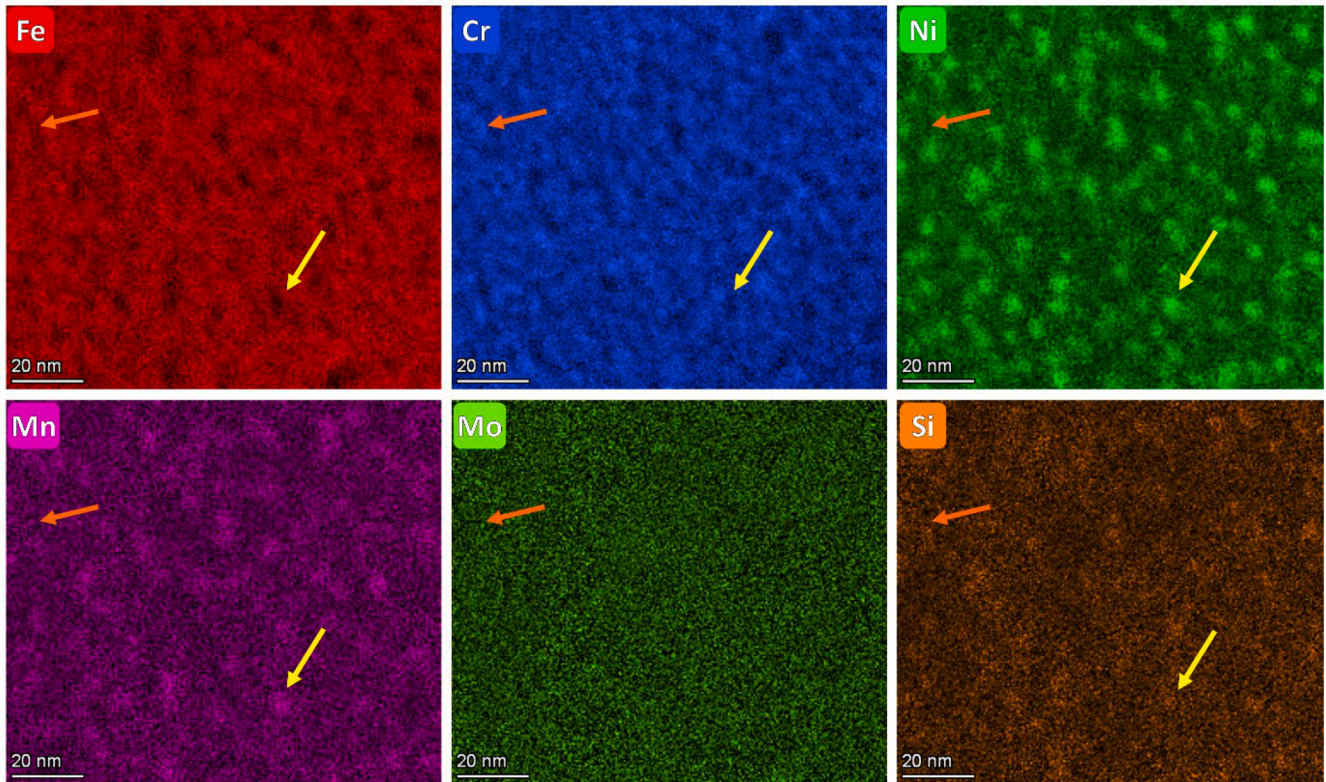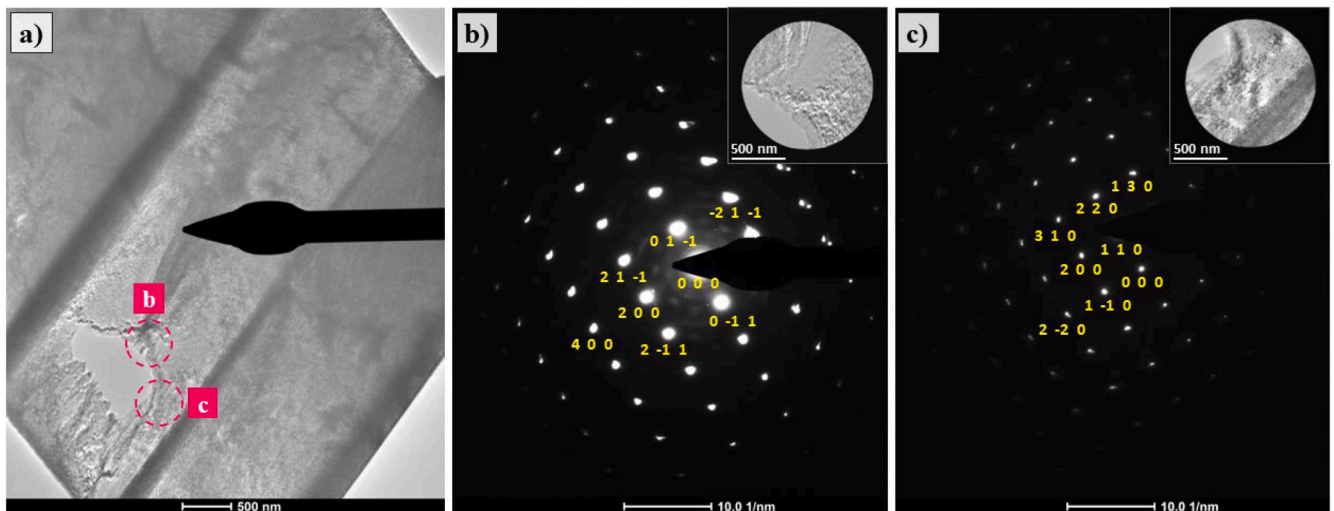

Fig. 9. The Ni RDF of 2209- DED-LB/w samples after 10, 50, and 1000 h aging at 400 °C.

Fig. 11. TEM-EDS elemental distribution maps of Fe, Cr, Ni, Mn, Mo, and Si in the ferrite of the DED-LB/w sample after 1000 h aging at 400 °C. The clustering, or precipitation, of G-phase is clearly seen in the Ni signal. The Cr and Fe maps show spinodal decomposition.

Fig. 12. a) TEM image of the thin foil extracted from the ferritic region using FIB, and (b, c) selected area electron diffraction (SAED) patterns of the ferrite in the DED-LB/w sample after 1000 h aging at 400 °C along the [011] and [001] zone axis, respectively. No diffraction spots from G-phase could be observed.

particles precipitate within the ferritic matrix with a cube-on-cube orientation, as previously reported [14]. Therefore, when observing the matrix along the [011] zone axis, the crystal orientation of the G-phase should also appear as [011], and the (600), (400), (200), and (220) G-phase diffraction spots should appear at intermediate positions [7]. However, as depicted in Fig. 12, only diffraction patterns corresponding to the bcc ferritic matrix are observed. There are also some faint circles and spots around the (000) spot; these are diffuse scattering of unclear origin (surface oxides or contamination) and do not indicate the presence of any discernible phases. Moreover, the SAED pattern in

Fig. 12-b shows some additional spots far from the (000) spot. These could result from double diffraction, where electrons are first diffracted by one set of planes and then by another set, leading to additional spots near the primary diffraction spots.

It should also be mentioned that TEM analysis was specifically performed on the 1000-hour sample, as this duration was expected to reveal significant microstructural changes, including possible G-phase formation. Since no phase transformation was detected after 1000 h, extending TEM analysis to shorter aging times (10 and 50 h) was deemed unnecessary.

4. Discussion

4.1. Age hardening of duplex stainless steels

Before aging, the ferrite phase in the 2209-DED-LB/w sample exhibited higher hardness compared to the ferrite in 2205-wrought DSS plate. This elevated hardness in the DED-LB/w sample can be attributed to three main reasons. Firstly, in the DED-LB/w-DSS component in which the austenite content is less than 2%, the ferrite phase is enriched with nitrogen. As established by prior research [9], this nitrogen-enriched ferrite is full of chromium nitrides, which inherently exhibit notably higher hardness, consequently contributing to an overall increase in the hardness of the ferrite phase. Secondly, the higher hardness can also be due to residual stresses from the AM (DED-LB/w) process. The existence of residual stresses in DED-LB/w components is widely acknowledged in existing literature. Processes like welding and additive manufacturing inherently involve rapid heating and cooling cycles, leading to the development of residual stresses [9]. Finally, ferrite in the DED-LB/w component has higher Ni content compared to wrought 2205 which is effective in increasing the ferrite hardness.

Comparing the age hardening of ferrite between the 2205-wrought DSS plate and 2209-DED-LB/w sample after 10 h, it becomes evident that a higher Ni content accelerates the embrittlement at early stages in the DED-LB/w samples. This acceleration is particularly noticeable since at this point, there are not many Ni-Mn-Si-rich clusters present. The primary reason for this acceleration, therefore, is the higher degree of ferrite decomposition during the early stages of the age-hardening process. Zhou et al. [5] who also noted a more pronounced ferrite decomposition attributed to the higher Ni concentration.

Following the age hardening at 400 °C revealed that the hardness increase after 1000 h was 163 HV for the wrought material, whereas it was 215 HV for the AM material. This implies that beyond the inherent higher hardness of the DED-LB/w sample for all aging times, the age hardening effect on the ferrite phase is more pronounced in the AM part.

4.2. Comparison of APT and TEM analysis

In this study, the investigation of 475 °C embrittlement in DSS was conducted using APT and TEM. Several differences were observed between these two characterization methods.

Firstly, APT is better in analyzing the chemical composition of nanometric particles as it examines atoms individually. In contrast, TEM measures the chemical composition within an interaction volume, which may encompass more than just the particle itself, as the TEM foil is often thicker than the diameter of the particles. Consequently, TEM has the

drawback of overestimating the presence of matrix alloying elements within the particles, as it also evaluates the surrounding bulk material.

Secondly, TEM tends to depict shorter distances between two particles. This occurs because in a TEM-EDS map, the map originates from the TEM analysis of several layers, essentially constituting a projection of the 3D volume. In contrast, the map visually presents all the particles in a 2D format on the screen, disregarding the depth dimension. However, as shown in Fig. 13, in APT, it is possible to choose a very thin layer that closely approximates a genuine 2D elemental map.

Finally, it is important to note that APT is a destructive technique, making it impossible to re-analyze the same volume. Conversely, TEM allows for additional analysis to be performed in the same region. TEM also has a major advantage in that the crystal structure in principle can be determined by diffraction, and it is usually better in determining the size of precipitates.

4.3. Formation of Ni-Mn-Si-rich clusters

When DSS is exposed to 400 °C, the ferrite phase begins to decompose into two distinct phases: the Fe-rich phase (α) and the Cr-rich phase (α'). This decomposition occurs due to the presence of a miscibility gap in the Fe-Cr phase diagram. This decomposition leads to the diffusion of Fe into the α phase and Cr into the α' phase as shown in Fig. 14. In commercial DSSs, which include various alloying elements like Ni, Mn, Mo, and Si, alongside the diffusion of Fe and Cr, there is also the diffusion of these additional elements. Specifically, the α phase tends to expel Si atoms, while the α' phase tends to expel Ni atoms. This is in agreement with the findings of this study, as illustrated in Fig. 7, where an enrichment of Ni, Mn, and Si atoms is observed outside of the Cr-rich (α') phase. Therefore, at the interface of the α and α' phases, there is accumulation of Ni, Mn, and Si atoms. Several studies have documented the concurrent formation of intermetallic compounds, such as G-, R-, and χ-phases, alongside the spinodal decomposition of ferrite in DSS [7].

Many studies have explored the formation of G-phase in DSS. While the stoichiometric composition of G-phase is $Ni_{16}Si_7Ti_6$, it has been reported in literature that constituent metallic elements, i.e., Ni and Ti can be replaced by other elements like Mn, Cr, Fe, Mo, V, and Nb [15,16]. Therefore, there are G-phase forming elements at the interface of the α and α' phases. Takeuchi et al. [17] observed G-phase formation with a chemical composition of $Ni_{16}Mn_6Si_7$ resulting from neutron irradiation. Moreover, in another study, they identified G-phase with similar chemical composition during submerged arc welding of DSS [18]. According to the APT results in Fig. 8, the chemical composition of the particles does not reach to $Ni_{16}Mn_6Si_7$ even after 1000 h aging since they still have less than 5 atomic percent Fe and Cr. However, in a
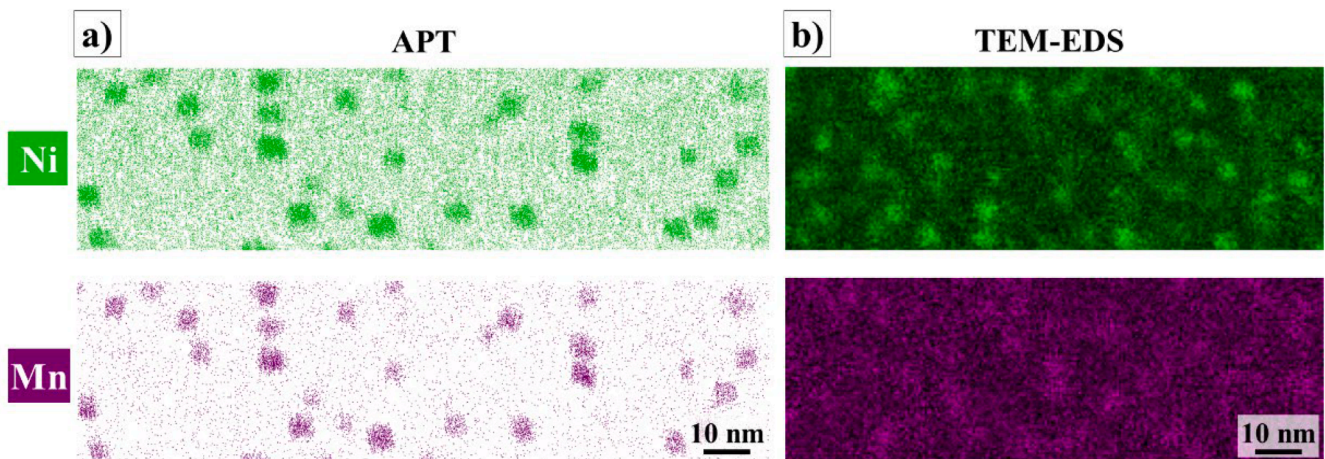
Fig. 13. a) 5 nm-thick slices of the APT analysis, and b) TEM-EDS maps of Ni and Mn in ferrite of DED-LB/w DSS after 1000 h aging at 400 °C. The apparent size of the particles is very similar for the two techniques.
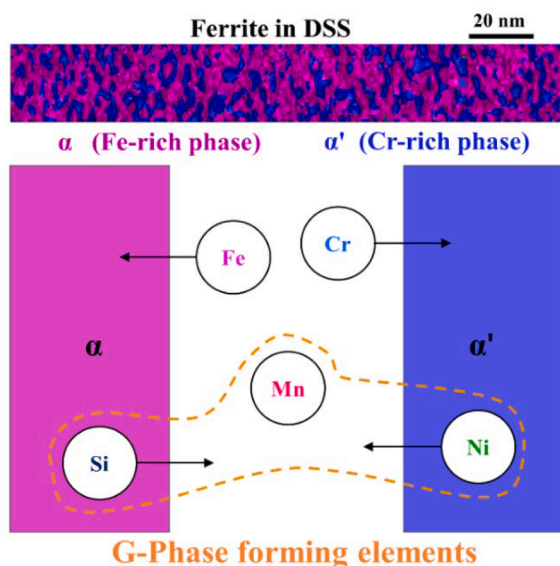
Fig. 14. A schematic representation of how ferrite decomposition into Fe-rich (α) and Cr-rich (α') phases can result in the enrichment of Ni, Mn, and Si in the intermediate area between these two phases.

comprehensive study regarding G-phase formation, Matsukawa et al. [7] introduced a two-step nucleation process. The first step involves the accumulation of Ni, Mn, and Si atoms, followed by the growth of these clusters. Growth and enrichment of these clusters occur simultaneously until they reach a critical size for structural changes. In the second step, while the cluster size remains nearly constant, matrix elements, namely Fe and Cr, begin to exit the clusters, being replaced by Ni, Mn, and Si atoms. When the cluster composition approaches the critical composition of $Ni_{16}Si_{3.5}(Fe,Cr)_{3.5}Mn_6$, the transformation from bcc ferrite to fcc G-phase takes place. The transformation requires an incubation period, which is influenced by factors like composition, grain size, and residual stresses within the parent ferrite grains.

In this study, even though there was the enrichment of Ni, Mn, and Si atoms in the clusters after 1000 h, the TEM diffraction patterns did not show any clear evidence of G-phase formation. There are two potential explanations for this observation; the G-phase formation had not occurred, or G-phase was not detected. Here, both possibilities are discussed.

Firstly, according to Matsukawa et al. [7], G-phase formation involves two distinct steps. While the chemical composition of the center of the clusters may have reached the critical composition of $Ni_{16}Si_{3.5}(Fe,Cr)_{3.5}Mn_6$, it is plausible that the incubation time was insufficient for G-phase formation to take place. Matsukawa et al. [7] also claimed that while the precipitation of Ni-Mn-Si-rich clusters initiates after 500 h of aging, the change in crystal structure becomes evident only after an extended aging period of 10,000 h. They also argued that the formation of G-phase necessitates the creation of an adequate number of vacancies. Consequently, a substantial quantity of vacancies must be generated and diffuse to the Ni-Mn-Si-rich clusters to facilitate the formation of G-phase. Furthermore, Mateo et al. [14] have indicated that the formation of G-phase is influenced by the concentration of Si. This observation aligns with the current study, where the Si concentration within the Ni-Mn-Si-rich regions was lower than what is typically associated with G-phase formation.

Another possibility is that G-phase indeed formed but was not detected. There are several reasons for not detecting G-phase. Firstly, based on the APT results, the radius of the largest Ni-Mn-Si clusters is only about 3.7 nm after 1000 h of aging. Moreover, as depicted in Fig. 10, the majority of these clusters (more than 80%) have a radius of less than 3 nm, possibly rendering them too small to be identified by

TEM. Hamaoka et al. [19] similarly reported that very small precipitates, which were not observable via TEM, could be detected by APT. They noted that although at longer aging times, such as 5000 h, all clusters of Ni-Mn-Si-rich material could be observed by TEM, at shorter aging times like 2000 h, it became challenging to perform TEM observations of these extremely small clusters. Chen et al. [20] reported the formation of G-phase within the ferrite phase after 1000 h of aging at 475 °C, as evidenced by TEM imaging. However, the detection of diffraction patterns proved challenging due to the limited volume of G-phase within the ferrite matrix, and there were only ferrite spots in the diffraction pattern. Secondly, if matrix elements such as Fe and Cr occupy the positions of Si and Mn atoms in G-phase, it could lead to weakening or disappearance of G-phase diffraction patterns [20]. In this study, even after 1000 h of aging, as depicted in Fig. 8-b, a considerable amount of Fe and Cr atoms are still observed within the Ni-Mn-Si-rich clusters. Consequently, these matrix elements might contribute to the obscuration of G-phase diffraction patterns.

4.4. 475 °C-embrittlement

In the binary Fe-Cr system, the age hardening of ferrite is primarily attributed to the decomposition of ferrite into Fe-rich (α) and Cr-rich (α') phases. However, in the presence of additional alloying elements such as Ni, Mn, Mo, and Si, the formation of intermetallic phases like G-, R-, and χ-phases becomes an important contributor to the age hardening. Consequently, comprehending the interplay between these two phenomena is crucial for mitigating the occurrence of 475 °C embrittlement in DSS.

In spinodal decomposition, the mismatch between the lattice parameters of α and α' phases is the main factor contributing to the embrittlement of the ferrite. While in the presence of Ni-Mn-Si- rich clusters or G-phase particles, precipitation hardening could be the main mechanism for embrittlement. Several studies have underscored the role of spinodal decomposition and G-phase formation in the age-hardening of DSS.

While in many studies, spinodal decomposition is considered as the main contributor to age hardening, Badyka et al. [21] and Sakata et al. [3] claimed that G-phase or Ni-Mn-Si-rich clusters can play a more pronounced role in age hardening.

To comprehend the extent of embrittlement resulting from spinodal decomposition, the Ardell model [22] offers a valuable framework. However, this model is applicable when spinodal decomposition is the sole embrittlement mechanism at play. In contrast, when embrittlement is driven by particles, two models come into consideration: the Orowan model [23] and a modified version of the Bacon, Kocks, and Scattergood (BKS) model [24]. These models are based on the interaction of dislocations with particles, and the presence of spinodal decomposition can affect dislocation movement towards these particles, making these two models inapplicable in this study.

Discussing the phenomenon of spinodal decomposition, a noteworthy trend can be observed in Table 2. During the initial phases of aging, the amplitude of spinodal decomposition experiences a rapid increase. However, with the progression of aging, it eventually stabilizes into a semi-equilibrium state. Simultaneously, the wavelength of spinodal decomposition begins to increase. This behavior can be attributed

Table 3
The wavelength and amplitude of ferrite decomposition into Fe-rich and Cr-rich phases in DED-LB/w-DSS compared to weld and base metals.

Material	Aging condition	Wavelength (nm)	Amplitude (at. %)
DED-LB/w -2209	400 °C, 1000 h	8.4	14.6
WM 2209 [3]	400 °C, 1000 h	4.9	6.9
BM 2205 [3]	400 °C, 1000 h	3.4	4.7
WM 2209 [6]	427 °C, 1000 h	–	~ 26
BM 2205 [6]	427 °C, 1000 h	–	~ 18

to the finite quantity of Cr atoms within the system.

Table 3 presents a comparative analysis of the wavelength and amplitude of spinodal decomposition in 2209 additively manufactured DSS compared to conventional 2209 weld metal and 2205 wrought materials. The results indicate that both the amplitude and wavelength of spinodal decomposition are notably higher in DED-LB/w-DSS compared to the weld and base metal. This increase can be attributed to the elevated Ni content in the ferrite, a consequence of the rapid cooling rates inherent to AM processes, particularly the DED-LB/w process. This higher Ni content serves to accelerate the spinodal decomposition, resulting in increased amplitude and wavelength.

Furthermore, it is important to acknowledge that the characterization techniques employed significantly influence the calculated amplitude and wavelength of spinodal decomposition. As discussed earlier, the inherent differences between TEM and APT analyses can introduce variability in these measurements, underscoring the importance of selecting the most appropriate technique for a given situation.

5. Conclusion

This study highlights the complex dynamics of age hardening and embrittlement in DSS with focus on an additively manufactured cylinder by DED-LB/w with higher Ni content. The APT and TEM analysis revealed the nanometric scale phenomena in the ferrite after aging at 400 °C up to 1000 h. The following conclusions can be drawn:

1. The 2209-DED-LB/w DSS cylinder sample exhibited initially higher hardness levels in its ferrite phase compared to 2205-wrought DSS plate.
2. The age hardening was more pronounced in the DED-LB/w component due to the higher Ni content.
3. Alongside the spinodal decomposition of ferrite into Fe-rich (α) and Cr-rich (α') phases, Ni-Mn-Si-rich clusters form at the interface of the α and α' phases.
4. While the Ni-Mn-Si-rich clusters could imply the nucleation of G-phase, the crystal structure of the G-phase was not detected, possibly due to the relatively short aging time or the limited capability of the characterization techniques.
5. The choice of characterization techniques, such as APT and TEM, significantly impacts the measurement results of spinodal decomposition. APT, while destructive, is adept at providing precise composition information for small clusters.

CRediT authorship contribution statement

Amir Baghdadchi: Writing – review & editing, Writing – original draft, Methodology, Investigation, Formal analysis, Data curation, Conceptualization. **Mattias Thuvander:** Writing – review & editing, Investigation, Formal analysis, Data curation. **Sten Wessman:** Writing – review & editing, Supervision, Conceptualization. **Boian T. Alexandrov:** Resources, Investigation, Conceptualization. **Joel Andersson:** Supervision, Resources.

Declaration of competing interest

The authors declare that they have no known competing financial interests or personal relationships that could have appeared to influence the work reported in this paper.

Acknowledgements

References

[1] F. Danoix, P. Auger, Atom probe studies of the Fe-Cr system and stainless steels aged at intermediate temperature: a review, Mater. Charact. 44 (2000) 177–201, https://doi.org/10.1016/S1044-5803(99)00048-0.

[2] Y. Fan, T.G. Liu, L. Xin, Y.M. Han, Y.H. Lu, T. Shoji, Thermal aging behaviors of duplex stainless steels used in nuclear power plant: a review, J. Nucl. Mater. 544 (2021), https://doi.org/10.1016/j.jnucmat.2020.152693.

[3] M. Sakata, K. Kadoi, H. Inoue, Mechanism for enhanced age hardening of 22% Cr duplex stainless steel weld metal fabricated with grade 2209 filler material, Mater. Today Commun. 33 (2022) 104201, https://doi.org/10.1016/j.mtcomm.2022.104201.

[4] A. Baghdadchi, C. Cary, N. Sridhar, M.A. Valiente Bermejo, C. Fink, J. Andersson, Corrosion resistance and microstructure analysis of additively manufactured 22% chromium duplex stainless steel by laser metal deposition with wire, J. Mater. Res. Technol. (2023), https://doi.org/10.1016/j.jmrt.2023.09.037.

[5] J. Zhou, J. Odqvist, M. Thuvander, S. Hertzman, P. Hedström, Concurrent phase separation and clustering in the ferrite phase during low temperature stress aging of duplex stainless steel weldments, Acta Mater. 60 (2012) 5818–5827, https://doi.org/10.1016/j.actamat.2012.07.022.

[6] D.A. Garfinkel, J.D. Poplawsky, W. Guo, G.A. Young, J.D. Tucker, Influence of alloying on α-α' phase separation in duplex stainless steels. Minerals, Metals and Materials Series, 2019, pp. 2399–2408, https://doi.org/10.1007/978-3-030-04639-2_161.

[7] Y. Matsukawa, T. Takeuchi, Y. Kakubo, T. Suzudo, H. Watanabe, H. Abe, T. Toyama, Y. Nagai, The two-step nucleation of G-phase in ferrite, Acta Mater. 116 (2016) 104–113, https://doi.org/10.1016/j.actamat.2016.06.013.

[8] A. Baghdadchi, V.A. Hosseini, M.A. Valiente Bermejo, B. Axelsson, E. Harati, M. Högström, L. Karlsson, Wire laser metal deposition additive manufacturing of duplex stainless steel components — development of a systematic methodology, Materials 14 (2021) 7170, https://doi.org/10.3390/ma14237170.

[9] A. Baghdadchi, V.A. Hosseini, M.A. Valiente Bermejo, B. Axelsson, E. Harati, M. Högström, L. Karlsson, Wire laser metal deposition of 22% Cr duplex stainless steel: as-deposited and heat-treated microstructure and mechanical properties, J. Mater. Sci. 57 (2022) 9556–9575, https://doi.org/10.1007/s10853-022-06878-6.

[10] M. Sakata, K. Kadoi, H. Inoue, Acceleration of 475 °C embrittlement in weld metal of 22 mass% Cr-duplex stainless steel, Mater. Today Commun. 29 (2021) 102800, https://doi.org/10.1016/j.mtcomm.2021.102800.

[11] H.J. Lee, B.S. Kong, G. Obulan Subramanian, J. Heo, C. Jang, K.S. Lee, Evaluation of thermal aging of δ-ferrite in austenitic stainless steel weld using nanopillar compression test, Scr. Mater. 155 (2018) 32–36, https://doi.org/10.1016/j.scriptamat.2018.06.016.

[12] J. Zhou, J. Odqvist, M. Thuvander, P. Hedström, Quantitative evaluation of spinodal decomposition in fe-cr by atom probe tomography and radial distribution function analysis, Microsc. Microanal. 19 (2013) 665–675, https://doi.org/10.1017/S1431927613000470.

[13] D. Tomus, H.P. Ng, In situ lift-out dedicated techniques using FIB-SEM system for TEM specimen preparation, Micron 44 (2013) 115–119, https://doi.org/10.1016/j.micron.2012.05.006.

[14] A. Mateo, L. Llanes, M. Anglada, A. Redjaïmia, G. Metauer, Characterization of the intermetallic G-phase in an AISI 329 duplex stainless steel, J. Mater. Sci. 32 (1997) 4533–4540, https://doi.org/10.1023/A:1018669217124.

[15] E.H. Lee, P.J. Maziasz, A.F. Rowcliffe, Structure and Composition of Phases Occurring in Austenitic Stainless Steels in Thermal and Irradiation Environments, Oak Ridge National Lab., TNUSA, 1980.

[16] D.S. Gelles, L.E. Thomas, Effects of Neutron Irradiation on Microstructure in Experimental and Commercial Ferritic Alloys, Hanford Engineering Development Lab., 1983.

[17] T. Takeuchi, Y. Kakubo, Y. Matsukawa, Y. Nozawa, Y. Nagai, Y. Nishiyama, J. Katsuyama, K. Onizawa, M. Suzuki, Effect of neutron irradiation on the microstructure of the stainless steel electroslag weld overlay cladding of nuclear reactor pressure vessels, J. Nucl. Mater. 443 (2013) 266–273, https://doi.org/10.1016/j.jnucmat.2013.07.035.

[18] T. Takeuchi, J. Kameda, Y. Nagai, T. Toyama, Y. Matsukawa, Y. Nishiyama, K. Onizawa, Microstructural changes of a thermally aged stainless steel submerged arc weld overlay cladding of nuclear reactor pressure vessels, J. Nucl. Mater. 425 (2012) 60–64, https://doi.org/10.1016/j.jnucmat.2011.12.004.

[19] T. Hamaoka, A. Nomoto, K. Nishida, K. Dohi, N. Soneda, Accurate determination of the number density of G-phase precipitates in thermally aged duplex stainless steel, Philos. Mag. 92 (2012) 2716–2732, https://doi.org/10.1080/14786435.2012.674222.

[20] Y. Chen, X. Dai, X. Chen, B. Yang, The characterization of G-phase in Fe20Cr9Ni cast duplex stainless steel, Mater. Charact. 149 (2019) 74–81, https://doi.org/10.1016/j.matchar.2019.01.012.

[21] R. Badyka, G. Monnet, S. Saillet, C. Domain, C. Pareige, Quantification of hardening contribution of G-Phase precipitation and spinodal decomposition in aged duplex stainless steel: APT analysis and micro-hardness measurements,

J. Nucl. Mater. 514 (2019) 266–275, https://doi.org/10.1016/j.jnucmat.2018.12.002.

[22] A.J. Ardell, Precipitation hardening, Metall. Trans. A 16 (1985) 2131–2165.

[23] A.K. Seeger, On the Theory of Radiation Damage and Radiation Hardening, Technischen Hochschule, Stuttgart, 1959. Max-Planck-Inst. fur Metallforschung.

[24] G. Monnet, Multiscale modeling of precipitation hardening: application to the Fe-Cr alloys, Acta Mater. 95 (2015) 302–311, https://doi.org/10.1016/j.actamat.2015.05.043.